DOI: 10.13009/EUCASS2019-328

A Combined Experimental and Computational Study of Jet Engine Combustion – Baseline Engine Operation

K. Danèl, N. Zettervall, T.E. Carlsson and C. Fureby
Defence Security Systems Technology, The Swedish Defence Research Agency
FOI, SE 147 25 Tumba, Stockholm, Sweden
kristoffer.danel@foi.se niklas.zettervall@foi.se torgny.carlsson@foi.se christer.fureby@foi.se

Abstract

In this investigation, we present results from combined jet-engine experiments in a recently developed facility, and numerical simulation results of the same jet engine using finite rate chemistry Large Eddy Simulation (LES) based on a recently developed skeletal mechanism for kerosene-air combustion. Both the experimental data and computational results reveal that this operating condition is a stable condition not experiencing any drift in the engine performance parameters or any thermoacoustic instabilities. The outlet temperature shows notable temporal and azimuthal variations reflecting the unsteady combustion and the number and location of the spray flames. The time- and area averaged outlet combustor temperature is in good agreement with the experimentally assessed global outlet temperature of the experiments. Furthermore, an FFT analysis of the predicted combustor pressure shows that the frequencies are grouped around three main frequencies centered at 540 Hz, 1120 Hz and 1735 Hz. This compares favorably with the corresponding experimental data of both the measured combustor pressure and the combustor light intensity emissions, having frequency peaks centered around 693 Hz, 1114 Hz. and 1792 Hz, respectively.

1. Introduction

For civilian and military aeropropulsion, including turboshaft engines for helicopters and small aircrafts, turbofans for large aircraft, and afterburning turbojets and turbofans for combat aircraft there is no realistic substitute for gas turbine engines. Modern aeropropulsion gas turbine engines are typically equipped with an annular combustor, with multiple burners sharing a common fuel supply line. Key factors affecting engine performance under normal operating conditions include velocity and temperature mean- and rms-pattern factors, combustor pressure drop, emissions, the ability to withstand thermoacoustic instabilities, flame extinction and blow-out, and the ability to relight at high altitudes, but also aspects such as thermal management and engine reliability are important. The trend in aeropropulsion gas turbine development is currently divided between a number of different high TRL technologies such as Rich-burn Quick-quench Lean-burn (RQL), Double Annular Combustor (DAC), Twin Annular Premixing Swirler combustors (TAPS) and Lean Direct Injection (LDI), as well as a number of low(er) TRL technologies including Lean Premixed Pre-vaporized (LPP), Axially Staged Combustors (ASC) and Variable Geometry Combustors (VGC) and the advancement is made incrementally rather than disruptively.

Combustion is typically maintained through a liquid fuel spray discharging into an annular combustor together with swirling air. This air is the main part of the air supplied by the compressor, whereas the remainder of the air is typically used to cool the combustor and to dilute the hot combustion products formed in the primary zone to achieve complete combustion and to lower the exhaust gas temperatures to levels that the turbine can withstand without excessive thermal loads. Neighbouring spray flames in an annular combustor interact with each other and with the pressure and flow fields in the combustor, which are in turn is affected by the air-flow through the, dilution, mixing and film cooling holes, resulting in a very complex combustor flow.

In order to understand and elucidate the combustion process in a jet engine, a detailed study must be undertaken on a representative engine under appropriate conditions. Ideally, this involves combined numerical and experimental studies, which, [1,2], also provide reciprocal validation of the tools used. This, in turn, poses great challenges regarding diagnostic access and computational capacity. Some aeroengine companies even have a flying test platform where the full envelope of the engine can be examined, [3]. To reduce costs during development and research, sub-system tests are typically performed at ground facilities, some facilities such as the AEDC test complex, [4], can test complete aeroengines in a large part of their envelope however, the experiments usually target a sub-systems such as the compressor or the internal flow path, [5]. For combustion purposes a combustion test rig is normally used, [6,7], and isolated phenomena can be studied and characterized. Here, the phenomena involved in the combustion process such as flow, fuel atomization, chemical reactions and heat-transfer can be studied separately. However despite

DOI: 10.13009/EUCASS2019-328

the possibility of controlling the boundary conditions it is still challenging to replicate the true conditions in a full-scale aeroengine where all the subsystems interact.

Current steady-state combustion Reynolds Averaged Navier Stokes (RANS) models, e.g. [8,9], cannot deal accurately with unsteady flow of this complexity. A more accurate but more expensive approach is to use combustion Large Eddy Simulation (LES), [10-12], in which the large scales of the flow are explicitly simulated and only the small (subgrid) scales are modeled, [13]. Practical combustion LES has now matured, so that single sector combustors are routinely studied, [2,14], whereas only a few multi-sector, fully annular, gas turbine combustor LES, capturing all acoustic modes and interactions, have been performed, [15-17]. Most of these single sector and multi-sector LES gas turbine combustor studies employ global one- or two-step reaction mechanisms, [15,16], although it is known, [18], that incorporation of more detailed reaction mechanisms, such as skeletal reaction mechanisms, is important. Several detailed reaction mechanisms are available for kerosene and kerosene surrogates, [19-22], as well as a few global mechanisms such as [23-25], but only very few skeletal reaction mechanisms, e.g. [26], has been developed that are suitable for LES of jet engine combustor studies.

In this study we will report on the experimental capability build-up in the area of jet engine combustion in support of existing computational studies. Particular focus is on developing a joint capability based on experimental and computational studies, using well-validated computational methods and purpose-build diagnostics based on well-characterized techniques. This capability will provide additional insight into gas turbine combustion, including thermoacoustics, off-design operating conditions, and ignition and light-around.

2. Experimental setup and measurement methodology

2.1 Test facility

In this section we briefly describe the FOI jet-engine experimental facility, the typical experimental set-up and the diagnostics used to investigate the baseline operating conditions.

The FOI jet engine test facility enables static testing of small jet engines at atmospheric conditions and includes performance testing of a complete engine as well as subphenomena or subcomponent tests (e.g. combustion and combustor). The ground level test cell is a 20 m^2 reinforced concrete room specially designed for propulsion experiments consist of an engine test stand, an inlet filter, fuel supply system data acquisition and a FADEC type control system. The test cell is also equipped with video monitoring and pressure and temperature probes

The test stand is mounted to a concrete foundation allowing the test object to be centrally mounted in the cell. At the front opening an air filter is mounted. The filter also serves to impose a pressure drop sufficiently large to break up in inflowing air stream tube forcing the air to enter the air inlet bellmouth more radially and alleviating the risk of ground vortex formation. The control system is in-house developed based around a National Instruments cRIO-9068 chassi. The system is built up as a full authority digital control system constantly monitoring critical values and allowing the user to select set points of either fuel pressure corrected rpm or corrected air mass flow rate. The start sequence is fully automated and has been optimized based on numerous tests. The current diagnostic setup includes 63 measurement points sampled at several different sampling rates and acquired by a common National instruments PXI-1085 chassi providing a common time-stamp. The system is capable of sampling rates up to 103 kHz. An optical arrangement allows access for a high-speed camera (Photron SA5) through one of the igniter holes directly in to the combustor chamber. This provides studies of the flame dynamics and the spatially and time resolved intensity variations of the chemiluminescence.

2.2 Experimental methodology

The objective of the performance tests are to obtain data reflecting the operational envelope of the engine and to acquire data for comparison with simulations. All the nomenclature and station numbering follows the ARP 755 guidelines [27]. For a jet-engine there exist a number of performance parameters, and here focus has been on the following parameters: net thrust (FN), air mass flow rate (W), fuel mass flow rate (Wf31), specific fuel consumption (SFC), compres-sor pressure ratio (PI31), fuel air ratio (FAR), equivalence ratio (φ) and turbine exit temperature (TET). To compare performance parameters of runs at different atmospheric conditions, the parameters are corrected by reference values corresponding to conditions at standard ISA atmosphere P_{ref} = 101.325 kPa, and temperature T_{ref} = 288.15 K, such that the relative pressure is $\delta = P/P_{ref}$ and the relative temperature is $\delta = T/T_{ref}$. The corrected values are denoted by a superscript "*" and calculated according to: corrected rotational speed, $N^* = N/\sqrt{\theta}$, corrected thrust, $FN^* = FN/\delta$, corrected air mass flow rate, $W^* = W\sqrt{\theta}/\delta$, and corrected pressure, $P^* = P/\delta$.

Special emphasis has been attributed to accurately measuring the air and fuel mass flow rates since these parameters constitute the base for other performance parameters and provide boundary conditions to the simulations. The fuel mass flow is measured with a Krohne Optimass 6000 Coriolis mass flow meter providing an accuracy of 0.1% of actual measured value. The air mass flow rate is based on pressure, temperature and humidity measurements. The set-up of the air mass flow rate is based on equal area weighted pressure measurements in the in-flow tube and has

DOI: 10.13009/EUCASS2019-328

been realized in accordance with the guidelines found in [28-31]. Since the air mass flow rate through the engine is one of the most important engine performance parameters great care has been taken in the hardware design affecting the air inflow quality, such as engine position in test cell, air inlet filter, intake bellmouth design and the downstream intake tube. For the pressure measurements related to the air mass flow rate measurements, DRUCK-UNIK-5000 type transducers ware used. The accuracy of this type of transducer is 0.04% of full-scale. The air mass flow rate is determined by: $W = C_D \rho A|\mathbf{u}|$, where C_D is the discharge coefficient, ρ the air density and A the intake area. The discharge coefficient, C_D, can be obtained from [28] and is a function of the intake Reynolds number, which in turn depends on the discharge coefficient. An iterative scheme was adopted to calculate the discharge coefficient. The uncertainty was computed for number of mass flows covering the span of the engine operational envelope and varies between 4% and 1.5 % at low the lower end and at maximum nominal air mass flow rate respectively.

The data experimentally acquired consisted of global parameters such as thrust, air pressure and temperature, sampled at 1 kHz and below, served as basis for calculating the performance parameters. Besides the global parameters another set of data was acquired at 10 to 25 kHz. This high speed diagnostics consisted of high speed video recording through the top spark plug access hole and a set of nine pressure sensors placed with the sensor heads mounted flush to the internal surface of the combustor casing. The objective of these were to: study the flame morphology, identify the frequency content of the flame, and to investigate the risk of azimuthal thermoacoustic instabilities.

The high-speed transient pressure measurements acquired by eleven pressure transducers manufactured by Kulite of type XTEL190SM-10PSID, which measured a differential pressure up to 68 kPa. The remaining three sensors measure the absolute pressure level and are of model XTL-190M. The sensors were placed at two stations (33 and 34) in axial direction and four sections in the azimuthal direction. At one azimuthal position a third sensor was mounted upstream (station # 2) in the axial direction and provided a three sensor line. The positioning of the sensor around the combustor casing can be seen in Figure 1

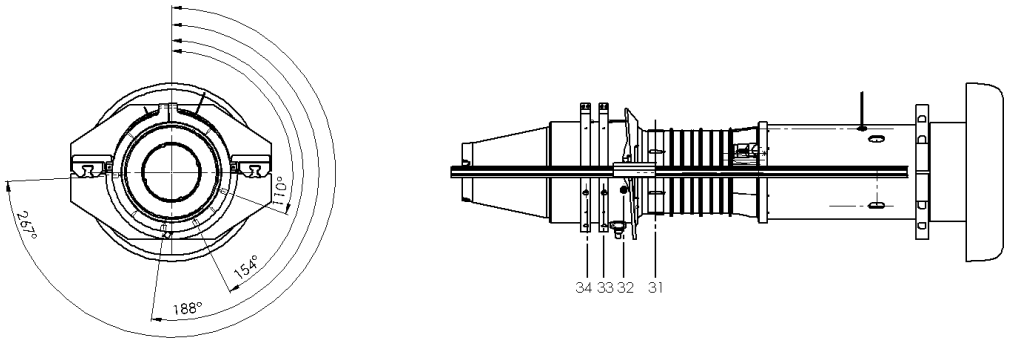

Figure 1: Positioning of the high speed pressure sensors.

To capture the dynamics of the flame, a high-speed imagining system was allowed access to the combustor through one of the ignitor holes, where a modified igniter casing, fitted with 25.4 mm diameter sapphire glass window allowed high transmissivity of the combustion chemiluminescence. Images of one of the twelve fuel injectors, Figure 2a and Figure 2b were recorded using a Photron SA5 and two camera lenses: one Leitz 90 mm lens placed backwards 200 mm away from the flame, and one Nikkor 105 mm 1:2.8 lens placed 300 mm further away attaching to the camera body via 31 mm spacer ring, the set-up can be seen in Figure 2c and Figure 2d where in the latter also a snapshot from a test is shown. The Photron Sa5 camera records 12 bit monochromatic images in the visible light spectra between 400 to 700 nm, and since CH* and C_2* have their emission peaks near 430 nm and 515 nm [32], respectively, it is most likely these two species that are detected in the images although OH* and CO_2* may also be detected as a weak background and a broadband emission over the full range of wavelengths. Excited species such as CH*, C_2* OH* and CO_2* are not usually included in any reaction mechanism, and in order to compare the LES with the experimental images CH and CO_2 are used instead. The full 1024x1024 pixel CCD of the camera was could be used up to 7000 frames per second, higher framerates reduced the number of pixels end hence the sensor area. 21000 frames per second showed to be a sufficient framerate for capturing the larger structures in the flame dynamics. Such image sequences were analyzed to investigate the flame structure and topology and to determine the frequency content of the light intensity. Each frame was divided into 25 square regions which constituted a base for the analysis of the intensity variations with respect to time and space. Each region in turn consisted of a cluster of pixels. The digital image (frame), denoted *D(r; t; u; v)* where *r* is indexing of the run number, *t* is time index, *u* is the index of pixels in the fuel ow direction and *v* is the index of pixels in the semi radial direction. *u* and *v* span the image plane. An initial assessment was to add all the pixel values in each frame together to form a single cell and only regard the time variance, $D(r,t) = \sum_u \sum_v D(r,t,u,v)$. The locations of the different cluster of pixels is shown in Figure 3, where the regions can be seen overlapping the engine structure. The background snapshot was taken using a disassembled test specimen and the ports

DOI: 10.13009/EUCASS2019-328

providing fresh air in to the combustor can be clearly seen. After the installation of the actual engine, the camera position was slightly shifted, resulting in a slightly modified image view denoted by the red rectangle.

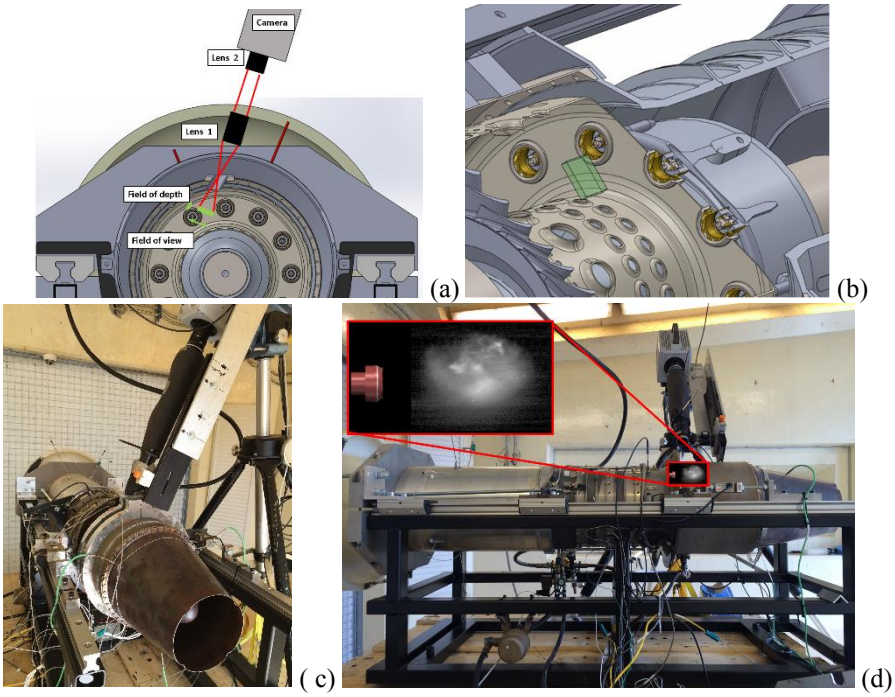

Figure 2: Position of the object plane (a) and (b) and, camera set up in the test cell (c) and (d). In (d) an image from the baseline operating condition is included.

The complete sequence of the binned images, each forming either a single or 25 super-pixels were then discretely transferred into the frequency domain using Welsh method, [33], based on Bartletts method, [34], i.e. $D(r,t) \rightarrow FD(r,f)$ and $D(r,t,j) \rightarrow FD(r,f,j)$, respectively. Here the *Welsh* method was used with a window function of type hamming, [55], and with a half window overlap. The window size was chosen to 1000 samples with a linear detrending.

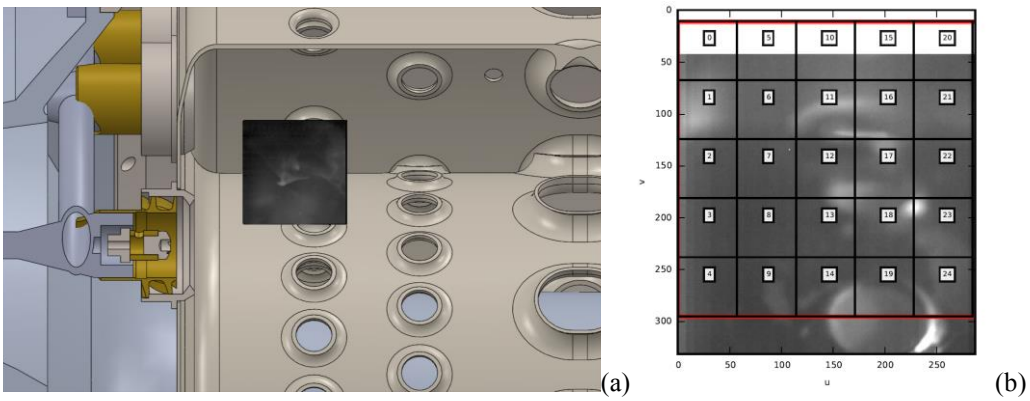

Figure 3 Position of the image plane of the digital image (a). The digital images were split up in 25 different regions. The background of this image is a snap shot taken using a disassembled engine, the red box indicates the actual area captured during the experiments (b).

3. Numerical simulations

3.1 LES models and numerical methods

As mentioned in the introduction there are two main branches of combustion LES: flamelet LES, e.g. [35-37], and finite rate chemistry LES, e.g. [11, 38-46]. Independently of branch, the governing equations are the low-pass filtered

DOI: 10.13009/EUCASS2019-328

equations of mass, momentum and energy representing convection, diffusion and chemical reactions. The low-pass filtering is used to separate the resolved scale flow (denoted by tildes and overbars, depending on if density weighted filtering or not is used) from the unresolved (subgrid) scale flow. The filtering is often implicit and implies that the physics on scales smaller than the filter width, Δ, must be represented by subgrid models, and physics on scales larger than Δ are explicitly resolved. For a linear viscous reacting mixture with Fourier heat conduction and Fickian diffusion the LES equations are,

$$\begin{cases} \partial_t(\bar{\rho}) + \nabla \cdot (\bar{\rho}\tilde{\boldsymbol{v}}) = 0, \\ \partial_t(\bar{\rho}\tilde{Y}_i) + \nabla \cdot (\bar{\rho}\tilde{\boldsymbol{v}}\tilde{Y}_i) = \nabla \cdot (D_i \nabla \tilde{Y}_i - \boldsymbol{b}_i) + \overline{\dot{w}_\iota}, \\ \partial_t(\bar{\rho}\tilde{\boldsymbol{v}}) + \nabla \cdot (\bar{\rho}\tilde{\boldsymbol{v}} \otimes \tilde{v}) = -\nabla \bar{p} + \nabla \cdot (2\mu\tilde{\boldsymbol{D}} - \frac{2}{3}\mu(\nabla \cdot \tilde{\boldsymbol{v}})I - B), \\ \partial_t(\bar{\rho}\tilde{E}) + \nabla \cdot (\bar{\rho}\tilde{\boldsymbol{v}}\tilde{E}) = \nabla \cdot (-\bar{p}\tilde{\boldsymbol{v}} + 2\mu\tilde{\boldsymbol{D}}\tilde{\boldsymbol{v}} - \frac{2}{3}\mu(\nabla \cdot \tilde{\boldsymbol{v}})\tilde{\boldsymbol{v}} + \kappa\nabla\tilde{T} - \boldsymbol{b}_E) - \tilde{q}_{rad}, \end{cases} \quad (1)$$

in which $\bar{\rho}$, $\tilde{\boldsymbol{v}}$, $\tilde{Y}_i$and $\tilde{T}$ are the filtered density, velocity, mass fractions and temperature, respectively, $\tilde{\boldsymbol{D}}$ the rate-of-strain tensor, $\bar{p} \approx \bar{\rho}R\tilde{T}$the pressure, R the gas constant, μ the viscosity, $D_i = \mu/Sc_i$the species diffusivity, $\kappa = \mu/\mathrm{Pr}$ the heat conductivity, in which Pr is the Prandtl and Sc_i the Schmidt number. The energy, $\tilde{E} = \tilde{\varepsilon} + \frac{1}{2}\tilde{\boldsymbol{v}}^2 + k$, is the sum of the internal energy, $\tilde{\varepsilon} = \tilde{h} - \bar{p}/\bar{\rho}$, the resolved kinetic energy, $\frac{1}{2}\tilde{\boldsymbol{v}}^2$, and the subgrid kinetic energy k, in which $\tilde{h} = \Sigma_i(\tilde{Y}_i(h_{i,f}^{\theta} + \int_{T_0}^{\tilde{T}} C_{p,i}dT))$ is the enthalpy, $h_{i,f}^{\theta}$the formation enthalpies and $C_{p,i}$ the specific heats.

The flow physics associated with the small, unresolved, eddies is concealed in the subgrid stress and flux terms $\boldsymbol{B} = \bar{\rho}(\widetilde{\boldsymbol{v} \otimes \boldsymbol{v}} - \tilde{\boldsymbol{v}} \otimes \tilde{\boldsymbol{v}})$, $\boldsymbol{b}_i = \bar{\rho}\left(\widetilde{\boldsymbol{v}Y_i} - \tilde{\boldsymbol{v}}\tilde{Y}_i\right)$ and $b_E = \bar{\rho}(\widetilde{\boldsymbol{v}E} - \tilde{\boldsymbol{v}}\tilde{E})$ that are here modeled utilizing the Localized Dynamic K-equation Model (LDKM), [47], in which $\boldsymbol{B} = \frac{2}{3}\mu_k(\nabla \cdot \tilde{\boldsymbol{v}})\boldsymbol{I} - 2\mu_k\tilde{\boldsymbol{D}}$, $\boldsymbol{b_i} = -\frac{\mu_k}{Sc_t}\nabla\tilde{Y}_i$ and $\boldsymbol{b}_E = -\frac{\mu_k}{Pr_t}\nabla\tilde{E}$, in which $\mu_k = c_k\bar{\rho}\Delta k^{1/2}$ is the subgrid viscosity, k the subgrid turbulent kinetic energy and Sc_t=Pr$_t$=0.7. Here, k is obtained from solving a modeled transport equation with dynamically computed coefficients following Kim & Menon, [47].

The combustion chemistry enters (**1**$_2$) through the filtered reaction rates, $\overline{\dot{w}_\iota} = M_i P_{ij}\overline{\dot{w}_j}$, with P_{ij} being the stoichiometric coefficients, M$_i$ the molar masses, and $\dot{w}_j = A_j T^{n_j} e^{-T_{A,j}/T}\Pi_{k=1}^{N}(\rho Y_k/M_k)^{b_k}$ the Arrhenius reaction rates. Here, A_j are the pre-exponential factors, $T_{A,j}$ the activation temperatures, n_j the temperature exponent and, b_j, the reaction order for reaction j. Based on previous investigations comparing different models for the filtered reaction rates, $\overline{\dot{w}_\iota}$, e.g. [48-51], we here use only the Partially Stirred Reactor (PaSR) model, [40], as this model appears to be one of the most robust, accurate and cost effective models given a range of test cases. More specifically, the PaSR model, [40], is based on essentially the same assumptions as the Eddy Dissipation Concept (EDC) model, [11], but the reacting volume fraction, γ*, is here estimated from theoretical estimates, [52], and DNS data, e.g. [53]. More recently, these approximations were supported, [54], by an extended analysis of the DNS data of Aspden *et al*., [55,56].

The spray is modeled assuming the spray consists of a homogeneous droplet distribution with the characteristic droplet time being estimated as $\tau_d = \rho_\ell d_d^2/18\mu$ in which ρ_ℓ is the liquid density, d_d the characteristic droplet diameter and ρ_ℓ the viscosity of the liquid. Furthermore, radiation is incorporated in the modeling using the P1-model, [57].

The LES equations are solved using a finite volume based code developed from the Open-FOAM C++ library, [58], which is based on an unstructured collocated finite volume method using Gauss theorem. The time-integration is performed with a semi-implicit second order ac-curate two-point backward differencing scheme, [59]. The convective fluxes are reconstructed using multi-dimensional cell limited linear interpolation, whereas diffusive fluxes are reconstructed using a combination of central difference approximations and gradient face interpolation. Here, a compressible version of the Pressure Implicit with Splitting of Operators (PISO) method, [60], is used to discretize the pressure-velocity-density coupling, using the thermal equation of state. The combustion chemistry is integrated separately, using a Strang-type operator-splitting algorithm, [61], together with a Rosenbrock time-integration scheme, [62,63], for the resultant systems of ordinary differential equations. The algorithm is second order accurate in space and time, and the equations are solved sequentially with a Courant number restriction of ~0.5..

3.2 Kerosene-air combustion chemistry

The fuel used in the experiment is JP-5 which is a kerosene grade fuel suitable for most aircraft engines. Such fuels have a carbon number between 8 and 16, and, following Ajmani *et al.*, [64], JP-5 is assumed to consist of C_8H_{18}, $C_{10}H_{22}$, $C_{12}H_{22}$, $C_{12}H_{24}$, $C_{14}H_{26}$ and $C_{16}H_{28}$ which can be represented by the average molecular formula $C_{12}H_{23}$. The

DOI: 10.13009/EUCASS2019-328

well characterized 65-step Z65 $C_{12}H_{23}$-air mechanism by Zettervall *et al*., [26], was here used to model the chemistry.

4. Results and discussion

In this Section we will first discuss the experimental and computational results individually, after which we will merge the two parts to provide a more comprehensive analysis combined with a reciprocal validation of the methods and models used in this investigation.

4.1 Global data from experiments

The performance data be presented in the following section are referred to an operational point set by the air mass flow rate. This parameter has been normalized by the manufacturer stated nominal design air mass flow rate, $W_{nom.}$ Other performance parameters are normalized with their corresponding nominal values.

Initial tests served to determine the required runtime for stationary operation of the engine with respect to heat soaking.. A 180 s heat soaking phase at N_{norm} = 0.86 was determined to be sufficient.A typical run is carried out with a start sequence ramping up to an initial rpm of approximately N_{norm} = 0.75, during 20-30 s followed by a heat soaking phase at approximately N_{norm} = 0.86 during 180 s. Then the desired operating conditions with respect to corrected thrust, corrected air mass flow or equivalence are set as a fixed value or a constant ramp. The performance parameters from three runs are presented in Figure 4. The runs #98 and #99had a constant positive ramps in fuel flow at two different rates (#99 medium rate, #98 low rate), whereas run # 97 consisted of high rate ramps up and down to a steady state corrected air mass flow rate. It can be seen in the top graph of Figure 4a that a minimum SFC occurs in between approximately 60% - 80% thrust. The bottom graph shows the relationship between corrected air mass flow rate and corrected thrust. The compressor performance can be defined by the isentropic efficiency and the compressor pressure ratio as a function of corrected air mass flow rate. During steady state operations at static thrust conditions the isentropic efficiency will form a line that represents its dependency on air mass flow rate. However at transient conditions or at different compressor loading these lines may shift. In Figure 4b graphs of the same three runs as previous are shown. As mentioned previously the consisted of different rate ramps of which run #97 had longer durations at constant corrected air mass flow (i.e. zero rate). These differences in rates results in offsetting the isentropic efficiency up when the ramp is positive and down when ramp is negative as can be seen in the top graph of Figure 4b. The red arrow in the top graph indicates increasing positive rate of change in the corrected air mass flow rate.

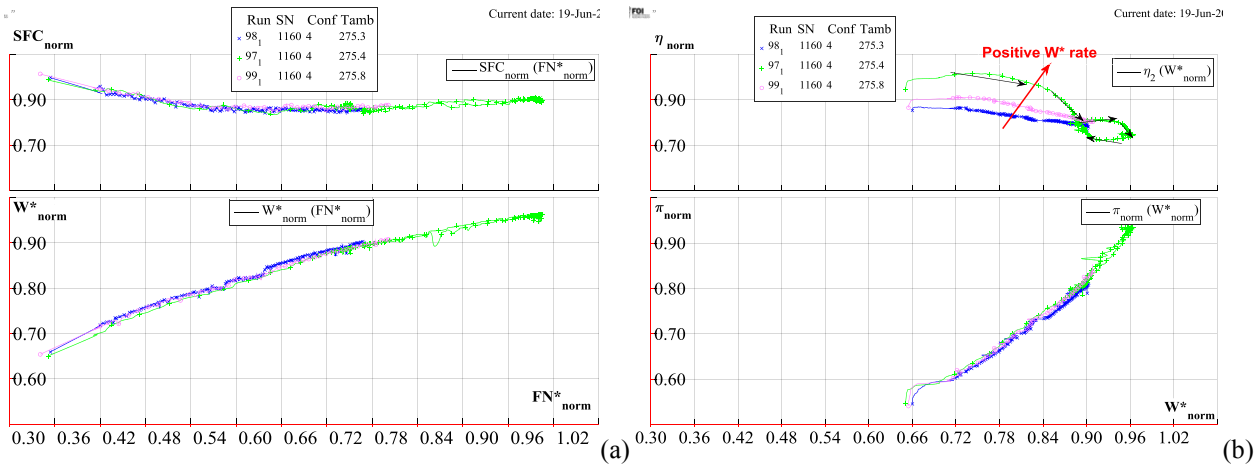

Figure 4: (a) Performance parameters of the engine as a function of normalized and corrected thrust, FN*. Top graph showing the normalized specific fuel and corrected normalized air mass flow rate in bottom graph. Data from three different runs, # 97 (-+), #98 (-x) & #99 (-o). (b) Compressor performance map of the engine, showing normalized performance data as a function of corrected air mass flow rate of the same runs as in (a). Isentropic compressor efficiency, top graph and compressor pressure ratio, bottom graph.

The compressor performance can be defined by the isentropic efficiency and the compressor pressure ratio as a function of corrected air mass flow rate. During steady state operations at static thrust conditions the isentropic efficiency will form a line that represents its dependency on air mass flow rate. However at transient conditions or at different compressor loading these lines may shift. These differences results in increasing the isentropic efficiency when the ramp is positive and decreasing it when ramp is negative as can be seen in the upper graph of Figure 4b. The red arrow in the upper graph indicates increasing positive rate of change in the corrected air mass flow rate. As seen

DOI: 10.13009/EUCASS2019-328

in the bottom graph of Figure 4b, the effect of the rate of change is not excessive. The transient condition when the engine is in a positive rate of change act as if the back pressure is larger than at a corresponding steady state condition. If a high enough rate is imposed the compressor would surge and the surge line could be identified. In compressor rig tests the back pressure is increased by a valve, [65], which provides better means of separating the relationship between pressure ratio and air mass flow rate which in turn allows identification of the surge line and choking of the compressor.

4.2 Unsteady experimental data

In Figure 5, the power spectral density is shown for all the nine differential pressure sensors at a steady state condition of the normalized corrected air mass flow rate corresponding to 0.97 (run log #71). In the left graph (a) frequencies up to the Nyquist criteria (~12 kHz) are shown, here it is observed that at a frequency above 10 kHz, the blade passing frequencies are dominating while the interesting region for the eigenmode frequencies is between 400 Hz and 6 kHz. The left graph (b) shows the same graph but with a frequency range up to 3.5 kHz. A simplified eigenmode analysis of the combustor showed that the first eigenfrequencies should occur in this range. At a closer inspection of the power spectra density peaks, four suspected eigenmode frequencies can be identified at approximately 610.4 Hz, 854.5 Hz, 1099 Hz and 1831Hz, respectively.

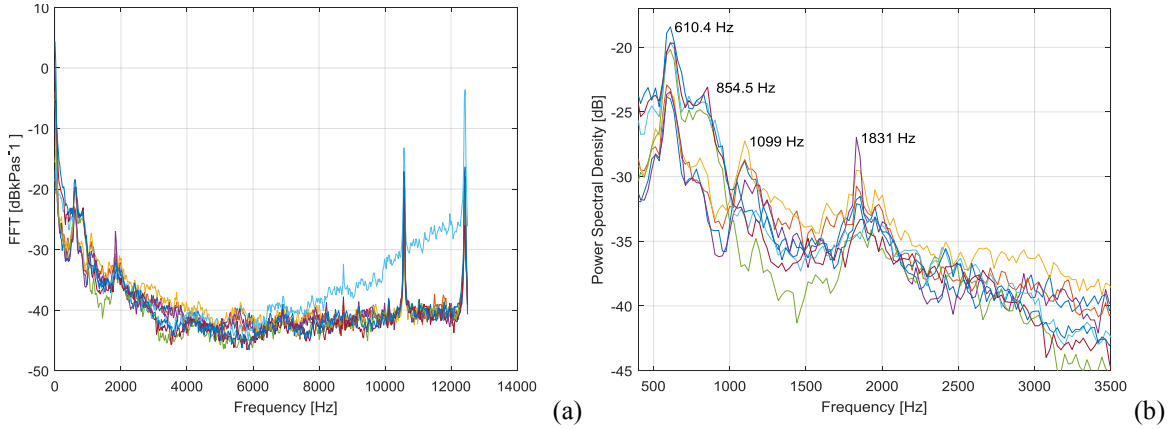

Figure 5: Frequency spectrum of all nine differential pressure gauges signals using Welch's power spectral density estimate. The peaks above10 kHz are related to the turbine blade passage seen in the left graph which spans up to the Nyquiest criteria (~12 kHz), while the frequency region related to the eigenmodes can be seen clearer in the right (b) graph, zoomed around 500-3500 Hz, the region for the first suspected eigenmodes. In graph (a) it is seen that one of the sensors displayed a higher sensitivity above 6 kHz (blue line).

The use of the high-speed non-intrusive diagnostics facilitates analysis of the spatial variation of the light intensity, and provides insight into the flame topology at various operating conditions. Figure 6a, shows the stacked images from run log#71 at identical conditions as presented above in the pressure frequency analysis. The resulting image represents the time integrated or summed amount of light in a particular region of the image plane. This enables "seeing trough the image". Visible in all these images is an intensity enhanced region located near j = 14 and j = 19. Looking back at Figure 3, it can be noticed that in this region large amount of fresh air is entering through the dilution hole visible at the bottom of the image. This position corresponds to the high intensity region (red) observed in zones 14 and 19. As with the pressure data, the image data was also analysed in the frequency domain. Regions j = [0; 5; 10; 15; 20; 1; 6; 11; 16; 21; 22; 23] showing low light intensity, have been discarded in this analysis due to their high signal-to-noise ratio. These regions are likely to produce an error prone result when forming the mean average of the FDs due to their poor signal-to-noise ratio. An average was formed based on all the remaining spectras. The averaging made use of normalized power spectras, *FD(r; f; j)*, and was performed by choosing a normalization value based on the mean value for all frequency components above 240 Hz. For the current operating condition it is difficult to find as clear frequency peaks as in the pressure data especially in the lower end of the spectra. Analyzing these frequency signals in greater detail, in particular by using a Butterworth band-pass filter and hence suppressing the lower and higher frequencies the dominating frequencies are: f≈290, 340, 420, 500, 580, 690, 820, 1100, 1800, 3070, 3350, 3500, 5750 and 7000 Hz.

Figure 6b presents the self-normalized mean power spectral density based on the light intensity variations, P_I, near the dilution hole corresponding to region 14 in Figure 6a, here represented by a solid blue line together with the associated self-normalized mean power spectral density based data from one differential pressure sensor, P_P. It is seen here that the resulting the power density of the light intensity is heavily shifted towards the lower end of the spectra.

DOI: 10.13009/EUCASS2019-328

The raw data for both signals has been treated similarly, using a 1st order bandpass Butterworth filter in the frequency range of 200<f<4000 Hz. When these signals are overlaid it can be observed that some of the peaks in the light intensity spectra correlates well with the pressure frequency peaks. These frequency peaks are centered around f=693, 1114 and 1792 Hz, respectively, and should thus be considered as the main frequencies of the unsteady flow, mixing and combustion features of this engine.

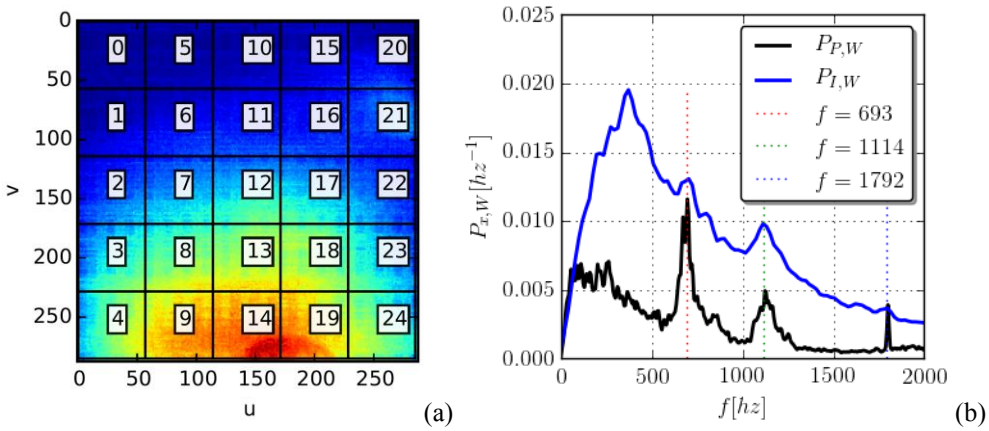

Figure 6: (a) Stacked image of a frame sequence providing a time integrated intensity.(b) Self-normalized mean power spectral density based on the light intensity variations near the dilution hole (—), Self-normalized mean power spectral density based data from one differential pressure sensor (—). The raw data for both modalities has undergone a bandpass Butterworth filter (f_{low}= 200, f_{high}=4000, order = 1).

4.3 Flame topology and emission spectra

One of the objectives of the high-speed video recordings was to obtain information about the flame topology. This proved to be a challenging task partially due the large amplitude in the light intensity variations combined with the sensitivity and dynamic range of the sensor and the three dimensional variations of the light intensity emitted from the flame. This three dimensional effect manifests itself as clouds being visible in- and out of focus, whereas other structures can be tracked in between frames. Nevertheless, at some time instances a somewhat clearer structure could be followed. In Figure 7a one such sequence is shown, the time in between frames is 47.6 µs and the integration time is 20. µs. It is difficult to determine any clear boundaries of a stable stationary flame, but one may track the evolution of high-intensity regions. In order to obtain an average all the images from one recording can be collapsed to one image, as presented in Figure 6a. Here a majority of the light emission is occurring near the primary port which is feeding fresh in to the combustor. Figure 7b shows the flame emission spectra from this region, the species attributed to the peaks are OH*, CH*, C_2* and Na*, the latter is believed to be trace elements and/or impurities in the fuel [32,66].

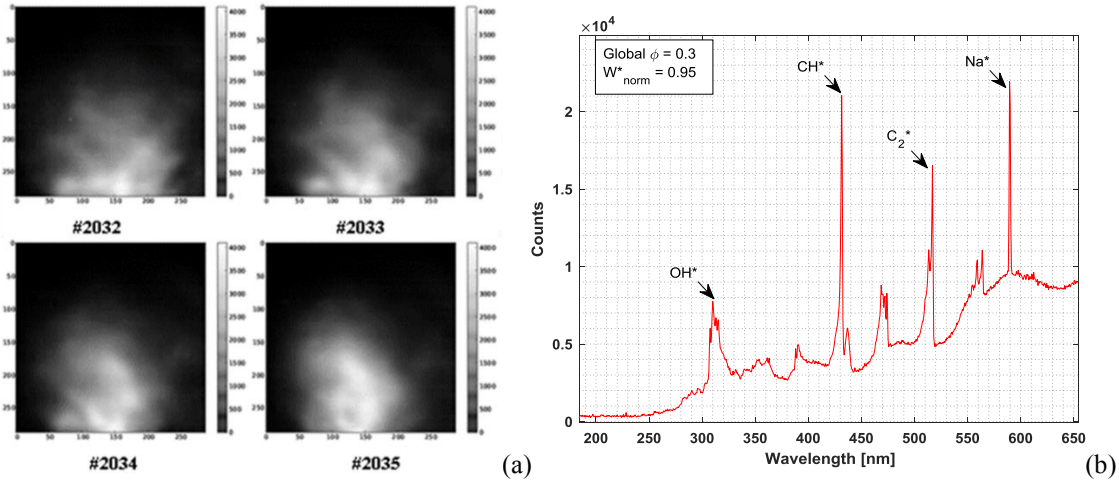

Figure 7: (a) Sequence of frames of the combustion process inside the combustor. Time between frames is 47.6 µs and the integration time is 20. µs. (b) Flame emission spectra recorded at a global equivalence ratio φ=0.3 and normalized corrected air mass flow rate W*$_{norm}$=0.95.

DOI: 10.13009/EUCASS2019-328

Figure 8 shows a schematic of the combustor in which the different burners and igniter holes are highlighted. The computational grid employed is composed of 52 million unstructured tetrahedral grid cells, figure 12b with cell sizes range from 0.2 mm in the fuel injector and swirler to 2.0 mm on the inner and outer combustor housing. The grid resolution is in-creased in parts with small details and/or high curvature. In addition, smooth transition in mesh size between different parts is carefully considered. Based on these settings the initial (patch-dependent) surface mesh is generated. The inlet air and fuel mass flow rates are specified together with the corresponding air and fuel temperatures. At the outlet a wave-transmissive boundary condition is used for the pressure whereas Dirichlet conditions are used for all other variables. The LES is started from uniform conditions corresponding to the inflow conditions and is this allowed to develop freely over ten flow through times before a fully developed flow is reached, and any statistical sampling started. A finer grid with 102 million cells is used to evaluate the grid sensitivity.

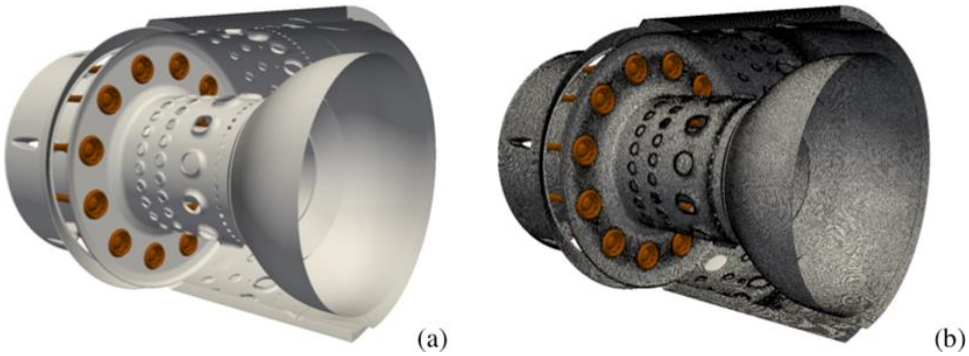

Figure 8 Perspective views of the combustor (a) geometry and (b) the computational grid. Key components of the combustor are highlighted

Figure 9a and Figure 9b present volumetric renderings of the temperature, T, the axial velocity, v_x, the heat-release, Q, and the liquid and gaseous fuel clouds, $Y_{C12H23}^{(l)}$ (purple) and $Y_{C12H23}^{(g)}$ (green). The axial velocity, v_x, reveals a topologically complex and interconnected recirculation region downstream of the burners and a multiply connected recirculation region between the flames and the dump plane. The cool jets entering the combustor can clearly be seen as well as the strong acceleration towards the end of the combustor and along the transition duct. The heat release, Q, primarily occur in the upstream part of the combustor with the air entering through the cooling holes providing a protective layer between the liner and the heat-release and the air entering through the large mixing holes cooling down the hot CO rich combustion products and providing additional air to facilitate the CO to CO_2 reactions. The temperature, T, shows large variations through the combustor, with notable decrease in T after the mixing holes. The highest T values are found in the upstream half of the combustor, where the liquid fuel is vaporized and most of the gaseous fuel is transformed into CO and intermediates and radicals, whereby most of the chemically stored energy is released. Towards the end of the combustor, and along the transition duct, the temperature decreases due to the injected cooling air, and the outlet temperature variation show noticeable azimuthal variations reflecting the positions of the flames and large mixing and dilution holes. The liquid fuel jets show large variations in shape as a consequence of the turbulent flow in the combustor and the pressure variations in the combustor, resulting in an unsteady Q distribution, which in turn affects the flow and the mixing, i.e. v_x and Y_i, and pressure, p. The main reason for the varying distribution is the variation in pressure, p, and in particular the azimuthal variations in p shown in Figure 10.

DOI: 10.13009/EUCASS2019-328

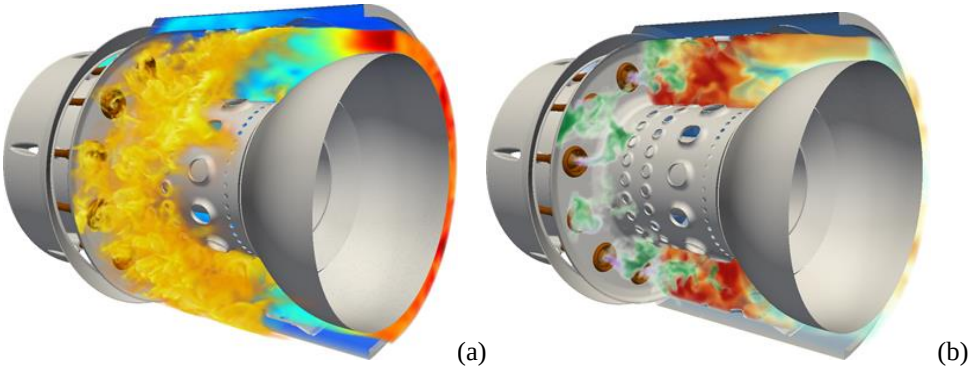

Figure 9 Volumetric renderings of the (a) axial velocity, v_x, combined with the heat-release, Q, and the (b) temperature, T, combined with the liquid and gaseous fuel distributions in purple and green, respectively. The color map for v_x range from semi-transparent blue to opaque red, and the mapping relating v_x with hue and opacity is linear. The color map for Q range from semi-transparent black to opaque white through red and yellow, and the mapping relating Q with hue and opacity is linear. The color map for T ranges from semi-transparent blue to opaque red, and the mapping relating T with hue and opacity is linear. The color map for the species ranges from semi-transparent white to the opaque color of the specie i, and the mapping relating Y_i with hue and opacity is linear.

Figure 10 presents unwrapped distributions of (b) v_x, (c) T, and (d) p, on the cylindrical surface in (a). The white line corresponds to the stoichiometric value of the mixture fraction, z_{st}. High v_x occur in the fuel jets and towards the transition duct whereas negative v_x typically occur between the fuel jets and in the most upstream third of the combustor. The recirculation region is composed of several recirculation regions dominating the upstream third of the combustor, creating a stable flame anchoring by recirculating high-temperature combustion products. The high-speed liquid fuel jets reveal a considerable spread in behavior, including velocity, penetration angle and depth, and are embedded in a strong swirling air stream. The T distribution is very fragmented, with the highest temperatures prevailing towards the end of the upstream half of the combustor, suddenly interrupted by the cold air from the mixing and dilution holes in the inner and outer liners. Due to the injection of cold air the temperature distribution develop streaks resulting in a very inhomogeneous temperature distribution at the combustor-turbine interface. The p distribution on this cylindrical plane shows a distinct azimuthal variation corresponding approximately to the 0x-1φ-0r eigenmodes of the combustor at 1703 Hz.

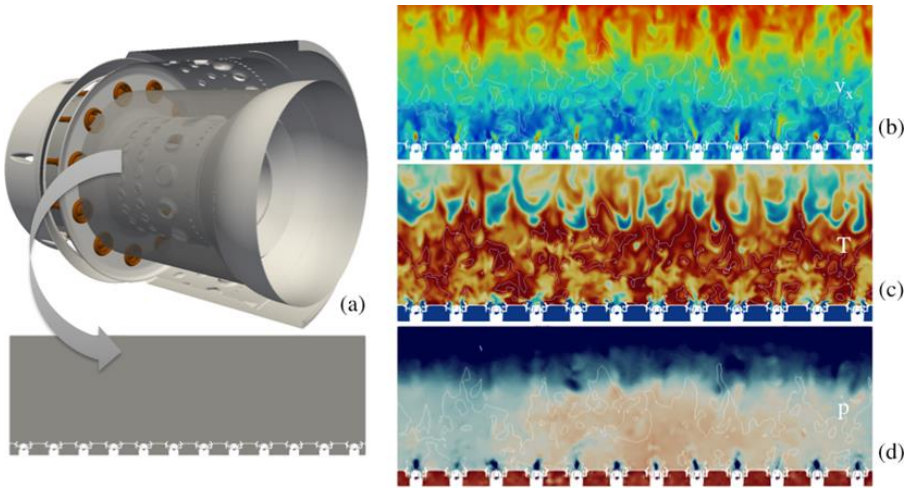

Figure 10: Unwrapped distributions of (b) axial velocity, v_x, (c) temperature, T, and (d) pressure, p, on the cylindrical surface in (a).

Supplementing the experimental results of the camera view, Figure 2, are the corresponding LES visualizations shown in Figure 11. As in the experiments the camera view for the LES results is looking in through one of the ignition holes of the outer combustor liner delimiting a box, Figure 11a, of equal size and location as the focal plan of the camera used in the experiments. In Figure 11b through Figure 11f instantaneous LES results of the velocity

DOI: 10.13009/EUCASS2019-328

vector field, ***v***, T, Q and species Y_{OH} and Y_{CH} are presented. As seen in Figure 11b ***v*** is dominated by the effects of volumetric expansion and turbulence, as is the case on the left hand side of the box, and the large volumes of cold air ingested from the cooling holes, as is the case on the top right corner of the box. In the left hand side of the box the flow is more turbulent due to the combined effects of the central and outer recirculation zones as well as the spray break-up and combustion. Furthermore, the flow is strongly three-dimensional as understood from the in- and out-of-plane velocity vectors. As seen in Figure 11c, T is strongly affected by the cooling flow through the liner as seen in the top right corner of the box. There is also a cooler center region of the box as a result of the three-dimensional flow from one of the nearby cooling holes. The heat-release distribution, Q, presented in Figure 11d in gray-scale to match that of Figure 7a, is clearly affected by both the strong three-dimensionality of the flow and the ingestion of cold air through the liner, but also by the production and consumption of the different species whose chemistry and reaction pathways are affected by the local equivalence ratio and the local temperature. This means that the reaction pathways and Q is affected by the local flow field and this also the liner geometry. In Figure 11e and Figure 11f instantaneous distributions of Y_{OH} and Y_{CH} are presented as they are the closest species available in the LES to the light emitting species OH*, CH* and C_2* producing the experimental images in Figure 7a. Both Y_{OH} and Y_{CH} agree reasonably well with Q in Figure 11d indicating that a large part of the light intensity is provided by the creation of OH* and CH*, represented by OH and CH in the LES, matching the combustion theory well. Note that a majority of Y_{CH} is located upstream of the burner (closest to the injectors). Here, the equivalence ratio is high and hence large amounts of Y_{CH} are expected. Further downstream, the equivalence ratio decrease due to the air entrainment diluting and cooling the mixture, and the amount of O_2 ingested enables the carbon species to convert into CO_2, mainly through reactions with OH.

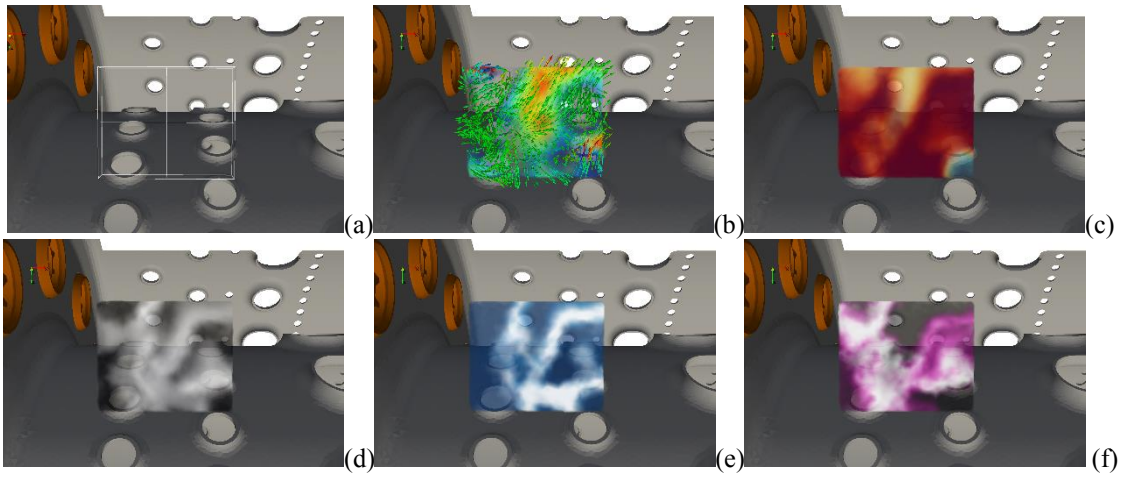

Figure 11: (a) View of the box used to represent the focal plan of the camera used in the experiments, (b) velocity vector field, **v**, (c) temperature, T, (d) heat-release, Q, (e) Y_{OH} and (f) Y_{CH}.

Figure 12a and Figure 12b show time traces of the pressure, p, and the heat-release, Q, respectively, in 23 sensors located on the different liner, dump-plane and casing surfaces of the combustor model. From the p time-series in Figure 12a we find that the p-traces form three groups oscillating around different mean pressure levels. The p-traces with the lowest mean pressure originate in the diffusor, whereas the p-traces with the intermediate mean pressure originate in the region between the inner and outer combustor casing and the combustor liner.

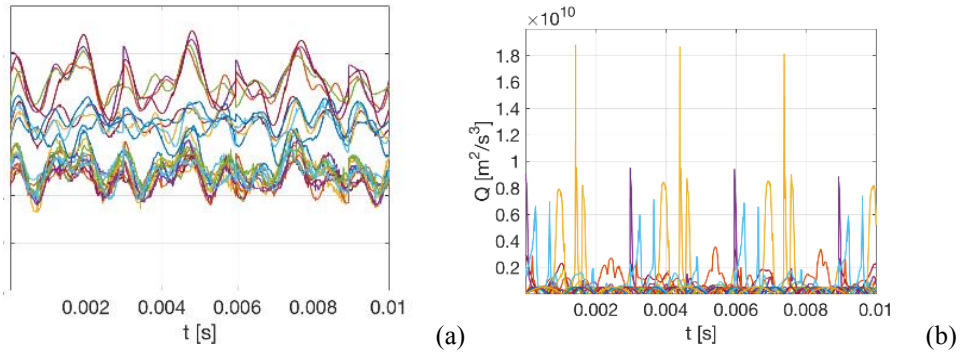

Figure 12 Time series analysis: (a) time-series of p at every 5th probe position and (b) time-series of Q at every 5th probe position.

DOI: 10.13009/EUCASS2019-328

Similarly, the p-traces with the highest mean pressure originate in the combustor. The corresponding Q-traces show a different behaviour with sharp peaks occurring with some regularity, in between which smaller peaks occur with less regularity. A number of probes are located in regions with zero or virtually zero Q. The associated Power Spectral Densities (PSDs) (not shown) reveal frequencies grouped around three main bands of 540 Hz, 1120 Hz and 1735 Hz, respectively. Comparing with the acoustic eigenmodes of the combustor (not shown) the second and third frequency bands are close to the 1/2x-0φ-0r eigenmode at 1168 Hz and the 0x-1φ -0r eigenmode at 1703 Hz, whereas the first frequency band corresponds approximately to the first longitudinal quarter wave mode. 1/4x-0φ -0r. Similar frequencies are also observed experimentally as described in Section 4.2. For Q, the frequencies are less well grouped, but appears to occur around 910 Hz, 1320 Hz, 1520 Hz and 1870 Hz. With respect to the Rayleigh criterion, we find from these time-series and PSDs that p and Q are generally not in phase, and hence the combustor should be stable, and thus not prone to combustion instabilities which is confirmed by the experimental analysis.

Figure 13a presents T at the combustor exit plane, whereas Figure 13b shows the radial variation of the radial and overall T-distribution factors, $RTDF = (\langle T_4\rangle_{\varphi,t} - \langle T_4\rangle_{r,\varphi,t})/(\langle T_4\rangle_{r,\varphi,t} - \langle T_3\rangle_{r,\varphi,t})$ and $OTDF = (T_{4,max} - \langle T_4\rangle_{r,\varphi,t})/(\langle T_4\rangle_{r,\varphi,t} - \langle T_3\rangle_{r,\varphi,t})$, which measures the inhomogeneities in T just upstream of the turbine. Here, $T_{4,max}$, $\langle T_4\rangle_{\varphi,t}$, $\langle T_4\rangle_{r,\varphi,t}$ and $\langle T_3\rangle_{r,\varphi,t}$ are the maximum exit temperature, mean azimuthal temperature, mean exit temperature and mean inlet temperature, respectively. As seen from Figure 13 the variation in T is significant and a number of high T patches can be observed, each essentially associated with one burner. However, the more complex T pattern observed is related to the unsteady flow and the weak helical flow pattern created by the co-rotating swirl from the burners. The RTDF and ODTF both quantifies the degree of heterogeneity seen by the turbine blades and needs to be controlled because of mechanical and thermal constraints. As expected, both RTDF and OTDF show similar profiles, and peak around 75% of the radial distance between the inner and outer liner walls. The average normalizedcombustor exit temperature is 0.95, which is in good agreement with the experimentally estimated value of 0.97, whereas the corresponding combustor normalized exit rms temperature fluctuations are 0.14.

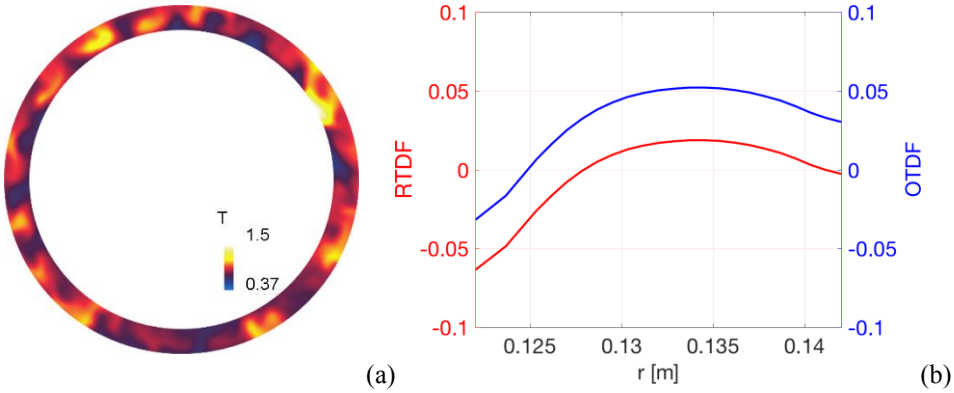

Figure 13: (a) Instantaneous temperature, T, distribution at the combustor exit plane and (b) the radial and overall temperature distribution factors, RTDF and ODTF, vs. the radial distance, r, between the inner and outer liner walls.

5. Concluding remarks

FOI has successfully commissioned a new test rig for aero propulsion studies. An investigation of the engine performance parameters at baseline operating conditions has been presented in this paper. Furthermore investigation targeting the combustion process here in conjunction with LES of the complete combustor including a 66 step skeletal chemical kinetic mode is also presented in this paper. The test setup provided steady state data of the performance characteristics of the engine and served as an input for the LES. A compressor map based on static tests within the envelope of the engine was established. The combustion study targeted the thermos acoustics inside the combustor at a normalized and corrected air mass flow rate corresponding to 0.97. A high speed (25000 fps) video recording system looking just downstream of one of the twelve fuel injectors together with nine differential pressure probes served to determine the frequency content of the flame intensity variations and pressure fluctuations. Here frequencies of the combustor pressure eigen modes were identified and showed at good match with both the light intensity variations and the frequency peaks based on pots processed data from the LES. The FOI LES codes have been previously benched and now showed a good agreement with respect to the frequencies of the post processed LES pressure data to both the experimental pressure data as well as the flame dynamics. This tells us that it can with confidence also be used to extract information to aid the understanding of the processes captured by the video recording. Here flow field, heat release and species concentration such as OH, CH and C_2H presented. The video footage showed that a major part of the light intensity is emitted in the area of the primary port flow which agrees well with the rendered images based on LES.

DOI: 10.13009/EUCASS2019-328

Acknowledgement

The authors acknowledge the financial support from the Swedish Armed forces, FOI staff: Stefan Olsson, Mattias Elfsberg and Leif Adelöw for their contribution to the experiments and Kevin-Nordin Bates for his work with the simulations.

References

[1] Noiray, N., and Schuermans, B. 2013. On the Dynamic Nature of Azimuthal Thermoacoustic Modes in Annular Gas Turbine Combustion Chambers. *Proceedings of the Royal Society*. Proc R Soc A, 469, p 20120535.

[2] Cannon, S. M., and Smith, C. E., 2003. LES PREDICTIONS OF COMBUSTOR EMISSIONS IN AN AERO GAS TURBINE,in *39th AIAA/ASME/SAE/ASEE Joint Propulsion Conference*, Huntsville, Alabama.

[3] Borg, , and Krejmas, A., 2000. Propulsion Flight Testing on General Electric's B747 Flying Test Bed,in *2000 World Aviation Conference*, San Diego, CA, pp. 2000-01-5523.

[4] Arnold Engineering Development Complex.2019, January [Online]. http://www.arnold.af.mil/library/factsheets/factsheet.asp?id=12977

[5] Wallin, F., Olsson, J., Peter, J., Kruger, E., Olausson, M., 2013. HIGH SPEED TESTING AND NUMERICAL VALIDATION OF AN AGGRESSIVE INTERMEDIATE COMPRESSOR DUCT,in *Proceedings of ASME Turbo Expo 2013: Turbine Technical Conference and Exposition*, San Antonio, Texas, USA, pp. GT2013-94315.

[6] Cochet, A. *et al.* 2016. ONERA Test Facilities for Combustion in Aero Gas Turbine Engines, and Associated Optical Diagnostics. *Aero-spaceLab Journal*, vol. AL11-01. Issue 11.

[7] Behrendt, T., and Hassa, C., 2006. A TEST RIG FOR INVESTIGATIONS OF GAS TURBINE COMBUSTOR COOLING CONCEPTS UNDER REALISTIC OPERATING CONDITIONS,in *25th Congress of International Council of the Aeronautical Sciences*, Hamburg Germany, pp. ICAS 2006-5.3.3.

[8] Poinsot, T., and Veynante, D. 2001 Theoretical and Numerical Combustion. Philadelphia: R.T. Edwards.

[9] Andreini, A. *et al.*, 2005. NOx Emissions Reduction in an Innovative Industrial Gas Turbine Combustor (GE10 Machine): A Numerical Study of the Benefits of a New Pilot-System on Flame Structure and Emissions,in *ASME Turbo Expo 2005: Power for Land, Sea, and Air*, vol. 2, Reno, Nevada, USA, pp. 235-247.

[10] Pitsch , H., and Duchamp De Lageneste , L., 2001. Large Eddy Simulation of Premixed Turbulent Combustion using a Level-Set Approach,in *Combustion Institute*.

[11] Fureby, C. 2008. LES Modeling of Combustion for Propulsion Applications. *Phil. Trans. R. Soc. A*, vol. 367, p. 2957.

[12] Olefin, C. J., Dozda, T. G., Sankaran, V. 2006. Large Eddy Simulation of Turbulence-Chemistry in Reacting Flows. *Journal of Physics: Conference Series*, vol. 46.

[13] Grinstein, F. F., Margolin, L., Rider, B. 2007 Implicit Large Eddy Simulation: Computing Turbulent Fluid Dynamics.: Cambridge University Press.

[14] di Mare, F., Jones, W. P., Menzies, K. R. 2004. Large Eddy Simulation of a Model Gas Turbine Combustor. *Combustion and Flame*, vol. 137. 3, pp. 278-294.

[15] Staffelbach, G., Gicquel, L. Y. M., Poinsot, T. 2007. "Highly Parallel Large Eddy Simulations of MultiburnerConfigurations in Industrial Gas Turbines," *Lecture Notes in Computational Science and Engineering*. 56, p. 325.

[16] Staffelbach, G., Gicquel, Y. M., Boudier, G., Poinsot, J. 2009. Large Eddy Simulation of self excited azimuthal modes in annular combustors. *Proceedings of the Combustion Institute* , vol. 32. 2, pp. 2909-2916.

[17] Zettervall, N., Worth, N., Dawson, J., Fureby, C. 2019. Large eddy simulation of CH4-air and C2H4-air combustion in a model annular gas turbine combustor. *Proceedings of the Combustion Institute*, vol. 37. 4, pp. 5223-5231.

[18] Bulat, G., Fedina, E., Fureby, C., Meier, W., Stopper, U. 2014. Reacting Flow in a Industrial Gas Turbine Combustor: LES and Experimental Analysis. *Proc. Comb. Inst.*, vol. 35.

[19] Dagaut, P., and Cathonnet, M. 2006. The ignition, oxidation, and combustion of kerosene: A review of experimental and kinetic modeling. *Progress in Energy and Combustion Science*, vol. 32. 1, pp. 48-92.

DOI: 10.13009/EUCASS2019-328

[20] LUCHE, J., REUILLON, M., BOETTNER, J.-C., CATHONNET, M. 2004. REDUCTION OF LARGE DETAILED KINETIC MECHANISMS: APPLICATION TO KEROSENE/AIR COMBUSTION. *Combustion Science and Technology*, vol. 176, pp. 1935-1963.

[21] Westbrook, C. K., Pitz, W. J., Oliver, H., Curran, H. J., Silke, E. J. 2009. A Comprehensive Detailed Chemical Kinetic Reaction Mechanism for Combustion of n-alkane Hydrocarbons from n-octane to n-hexadecane. *Combustion and Flame*, vol. 156. 1, pp. 181-199.

[22] Egolfopoulos, F. N. *et al.* 2010 A High-Temperature Chemical Kinetic Model of n-Alkane (up to n-Dodecane), Cyclohexane, and Methyl-, Ethyl-, n-Propyl and n-Butyl-Byclohexane Oxidation at High Temperatures - JetSurF version 2.0. [Online]. http://web.stanford.edu/group/haiwanglab/JetSurF/JetSurF2.0/index.html

[23] Franzelli, B., Riber, E., Sanjose, M., Poinsot, T. J. 2010. A two-step chemical scheme for kerosene–air premixed flames. *Combustion and Flame*, vol. 157. 7, pp. 1364-1373.

[24] Choi, J. Y., 2011. A Quasi Global Mechanism of Kerosene Combustion for Propulsion Applications,in *47th AIAA/ASME/SAE/ASEE Joint Propulsion Conference & Exhibit*, San Diego, Cal, pp. A2011-5853.

[25] Jones, W. P., and Tyliszczak, A. 2010. Large Eddy Simulation of Spark Ignition in a Gas Turbine Combustor. *Flow, Turbulence and Combustion*, vol. 85. 3-4, pp. 711-734.

[26] Zettervall, N., Fureby, C., Nilsson, E. J. K. 2016. Small Skeletal Kinetic Mechanism for Kerosene Combustion. *Energy Fuels*, vol. 30. 12, pp. 9801-9813.

[27] ASME. 2011. "Gas Turbine Engine Performance Station Identification and Nomenclature, Aerospace Recommended Practice ARP755A," Society of Automotive Engineers, Warrandale, Pennsylvania,.

[28] ASME. 2011. "ASME-MFC26-2011 Measurement of Gas Flow by Bellmouth Inlet Flowmeters," New York,.

[29] AGARD. 1991. Air intakes for high speed vechicles. *AGARD*. AR -270, pp. 417-442.

[30] AGARD. 1990. "AD-A226 378 Recommended Practises for Measurment of Gas Pressures and Temperatures for Performance Assesment of Aircraft Turbine Engines and Components," Essex,.

[31] SAE. 1994. "SAE-ARP1420, Gas Turbine Engine Inlet Flow Distorion Guidlines," Warrendale,.

[32] Seyfried, H., Richter, M., Aldén, M. 2007. Laser-Induced Phosphorescence for Surface Thermometry in the Afterburner of an Aircraft Engine. *AIAA Journal*, vol. 45. 12, pp. 2966-2971.

[33] Welch, P. D. 1967. The use of fast fourier transform for the estimation of power spectra: A method based on time averaging over short, modifed periodograms. *IEEE Transactions on Audio and Electroacoustics*, vol. 15. 2, pp. 70-73.

[34] Bartlett, M. S. 1948. Smoothing Periodograms from Time-Series with Continuous Spectra. *Nature*, vol. 161. 4096, pp. 686-687.

[35] Hawkes, E., and Cant, S. 2001. Implications of a flame surface density approach to large eddy simulation of premixed turbulent combustion. *Combustion and Flame*, vol. 126. 3, pp. 1617-1629.

[36] Peters, N. 2000 Turbulent Combustion.: Cambridge University Press.

[37] Ma, T., Stein, O. T., Chakraborty, N. 2013. A posteriori testing of algebraic flame surface density models for LES. *Combustion Theory and Modelling*, vol. 17. 3, pp. 431-482.

[38] Colin, O., Ducros, F., Veynante, D., Poinsot, T. 2000. A thickened flame model for large eddy simulations of turbulent premixed combustion. *Physics of Fluids* , vol. 12, p. 1843.

[39] Giacomazzi, E., Bruno, C., Favini, B. 2000. Fractal Modeling of Turbulent Combustion. *Proc. Comb. Inst.*, vol. 4, p. 391.

[40] Sabelnikov, V., and Fureby, C. 2013. LES Combustion Modeling for High Re Flames using a Multi-Phase Analogy. *Comb. Flame*, vol. 160, p. 83.

[41] Mathew, J. 2002. Large eddy simulation of a premixed flame with approximate deconvolution modeling. *Proceedings of the Combustion Institute*, vol. 29. 2, pp. 1995-200.

[42] Gerlinger, P. 2003. Investigation of an assumed PDF approach for Finite-Rate-Chemistry. *Combustion Science and Technology* , vol. 175, pp. 841-872.

[43] Pope, S. B. 1985. PDF Methods for Turbulent Reactive Flows. *Prog. Energy Comb. Sci.*, vol. 11, p. 119.

[44] Navarro-Martinez, S., Kronenburg, A., Di Mare, F. 2005. Conditional Moment Closure for Large Eddy Simulations. *Flow, Turbulence and Combustion*, vol. 75. 1-4, pp. 245-274.

[45] Echekki T; Mastorakos E, "The Linear-Eddy Model," in *Fluid Mechanics and Its Applications*.: FMIA, 2010, pp. 221-247.

DOI: 10.13009/EUCASS2019-328

[46] Dodoulas, I. A., and Navarro-Martinez, S. 2013. Large Eddy Simulation of Premixed Turbulent Flames Using the Probability Density Function Approach. *Flow, Turbulence and Combustion*, vol. 90. 3, pp. 645-678.

[47] Kim, W. W., and Menon, S. 1999. A New Incompressible Solver for Large Eddy Simulations. *Int. J. Num. Meth. Fluids*, vol. 31, p. 983.

[48] Fureby, C., 2017. A Comparative Study of Large Eddy Simulation (LES) Combustion Models applied to the Volvo Validation Rig,in *55th AIAA Aerospace Sciences Meeting*, Grapevine, Texas, pp. AIAA 2017-1575.

[49] Fureby, C., 2018. The Volvo Validation Rig – A Comparative Study of Large Eddy Simulation Combustion Models at Different Operating Conditions,in *AIAA Aerospace Sciences Meeting*, Kissimmee, Florida, pp. AIAA 2018-0149.

[50] Fedina, E., Fureby, C., Bulat, G., Meier, W. 2017. Assessment of Finite Rate Chemistry Large Eddy Simulation Combustion Models. *Flow Turbulence and Combustion*, vol. 99. 2, pp. 1-25.

[51] Fureby, C., Zettervall, N., Kim , S., Menon, S., 2015. LARGE EDDY SIMULATION OF A SIMPLIFIED LEAN PREMIXED GAS TURBINE,in *9th Int. Symp. on Turb. and Shear Flow Phen. (TSFP-9)*, Melbourne, Australia.

[52] Chomiak, J. 1979. Basic considerations in the turbulent flame propagation in premixed gases. *Progress in Energy and Combustion Science*, vol. 5. 3, pp. 207-221.

[53] Tanahashi, M., Fujimura, M., Miyauchi, T. 2000. Coherent Fine Scale Eddies in Turbulent Premixed Flames. *Proc. Comb. Inst.*, vol. 28, p. 5729.

[54] Aspden, A., Zettervall, N., Fureby, C. 2019. An a priori analysis of a DNS database of turbulent lean premixed methane flames for LES with finite-rate chemistry. *Proceedings of the Combustion Institute*, vol. 37. 2, p. 2301.

[55] Aspden, A., Day, M. S., Bell, J. B. 2016. Three-dimensional direct numerical simulation of turbulent lean premixed methane combustion with detailed kinetics. *Combustion and Flame*, vol. 166, pp. 266-283.

[56] Aspden, A., Bell, J. B., Egolfopoulos, F. 2017. Turbulence–flame interactions in lean premixed dodecane flames. *Proceedings of the Combustion Institute*, vol. 36. 2, pp. 2005-2016.

[57] Zhau, J. M., and Liu, L. H., "Radiative Transfer Equation and Solutions," in *Handbook of Thermal Science and Engineering*.: Springer Verlag, 2017.

[58] Weller, H. G., Jasak, H., Fureby, C. 1997. A Tensorial Approach to CFD using Object Oriented Techniques. *Computers in Physics*, vol. 12, p. 629.

[59] Lambert, J. D. 1973 Computational Methods in Ordinary Differential Equations. New York: Wiley.

[60] Issa, R. 1986. Solution of the Implicitly Discretized Fluid Flow Equations by Operator Splitting. *Journal of Computational Physics*, vol. 62. 1, p. 40.

[61] Strang, G. 1968. On the Construction and Comparison of Difference Schemes. *SIAM Journal on Numerical Analysis*, vol. 5. 3, pp. 506-517.

[62] Rosenbrock, H. H. 1963. Some General Implicit Processes for the Numerical Solution of Differential Equations. *The Computer Journal*, vol. 5. 4, pp. 329-330.

[63] Hairer, E., and Wanner, G., "Solving Ordinary Differential Equations," in *Stiff and Differential-Algebraic Problems 2nd Ed*.: Springer Verlag., 1991, ch. II.

[64] Ajmani, K., Yungster, , Breisacher, K., 2006. Chemical Kinetics Modeling for a Hydrocarbon Fueled Pulse Detonation Device,in *42nd AIAA/ASME/SAE/ASEE Joint Propulsion Conference & Exhibit*, pp. AIAA 2006-4791.

[65] Walsh, P. P., and Fletcher, P. 2004 Gas Turbine Performance. Bristol: Blackwell Publishing.

[66] Trindadea, T., Ferreira, A., Fernandes, E., 2013. Characterization of Combustion Chemiluminescence: an Image Processing Approach,in *Conference on Electronics, Telecommunications and Computers – CETC 2013*, Lisbon, Portugal, pp. 194-201.